

Research Article

Production of Methanol from Aqueous CO₂ by Using Co₃O₄ Nanostructures as Photocatalysts

Salvador Pocoví-Martínez , Inti Zumeta-Dube, and David Diaz 

Facultad de Química, Universidad Nacional Autónoma de México, Avenida Universidad 3000, Ciudad Universitaria, Coyoacán, CP 04510 Mexico City, Mexico

Correspondence should be addressed to Salvador Pocoví-Martínez; salvador.pocovi@hotmail.es and David Diaz; david@unam.mx

Received 18 June 2018; Accepted 2 October 2018; Published 9 January 2019

Academic Editor: Giuseppe Compagnini

Copyright © 2019 Salvador Pocoví-Martínez et al. This is an open access article distributed under the Creative Commons Attribution License, which permits unrestricted use, distribution, and reproduction in any medium, provided the original work is properly cited.

In this work, we report for the first time the photocatalytic activity of Co₃O₄ nanostructures for the reduction of aqueous CO₂ to methanol (MeOH). This could be considered a simple example of artificial photosynthesis. The photocatalysis experiments were developed under simulated solar light of 100 mW/cm² and without using any sacrificial agent. To carry out this study, nanostructured mixed valence cobalt oxide (Co₃O₄) powders, with porous nanoparticle aggregates of different morphologies, have been prepared by two synthesis methods. The characterization of structural (PXR, XPS, SEM, and TEM) and optical (UV-vis-NIR, Raman, and FT-IR) properties, magnetization curves, and surface area (BET) was accomplished.

1. Introduction

Global warming is the major issue that humanity has to face in the next 50 years. Some effects that could be devastating for humankind are the increase of global temperature, rise of sea level, extreme droughts, devastating floods, destructive storms, among others [1–5]. The reduction of gases that contribute to the Earth's surface warming can solve some problems that we are experiencing right now as the weather changes and the global temperature is rising. A great number of authors claim that the main cause of global warming is CO₂ [6–9]. Almost all the excess of this gas in the atmosphere is produced by the combustion of mineral fuels, like gasoline or coal. Many efforts have been done in the last years aiming to reduce CO₂ emissions to the atmosphere: imposition of taxes for CO₂ emissions, CO₂ sequestration using different methods [10–20], or the conversion of this gas using different techniques to obtain value added products, e.g., fuels [21–33]. In order to reduce CO₂ quantity in the atmosphere and produce fuels using this gas and water, different materials and methods have been applied: metal complexes [21], microalgae [28, 33], syngas procedure [24], polymers [31], electrochemical transformations [26, 32],

photothermal and thermochemical conversions [23, 25], semiconductors [27, 30], and several others.

One of the most attractive ways of producing fuels from CO₂ and water is through photocatalytic semiconductor-mediated solar energy conversion. This fascinating fundamental and technological problem has challenged the scientific community for many years. A great variety of semiconductors, sometimes combined with metal nanostructures, carbon-based materials, and/or organometallic molecules have been tested with the mentioned purpose, and important progresses have been reached [34]. However, typical semiconductors with an adequate band gap for solar energy absorption (Si, CdSe, CdTe, GaAs, GaP, PbS, SbS, among others) are unstable in contact with electrolytes, and those with higher stability (TiO₂, ZnO, SnO, ZnS, inter alia) cannot absorb a huge component of solar radiation [35]. A group of semiconductors, such as CuO, Fe₂O₃, or BiVO₄, display both a wide spectral range of solar light absorption as well as stability when in contact with aqueous solutions of electrolytes. This last group of semiconductors has been largely studied in photocatalytic water splitting and/or CO₂ photoreduction [36]. Another interesting semiconductor is Co₃O₄; it is stable in aqueous

suspensions and oxygen-rich atmospheres and thus can be prepared and easily manipulated under usual laboratory conditions. This material has unique optical properties because it shows several band gaps in different regions of the electromagnetic spectrum (0.7–4.4 eV) [37–39]. Because it absorbs light in the UV, visible, and infrared regions, it can be a good candidate to carry out photocatalytic reactions when Co_3O_4 interacts with light. In addition, the preparation of different sizes and shapes of this material could potentially enhance the photocatalytic activity, since the optical properties may change and the area and surface defects of the material can increase with regard to its bulk counterpart. Despite the ad hoc properties of this material, only two studies have been reported regarding nanostructured Co_3O_4 as an active photocatalyst for CO_2 reduction [40, 41]. Formic acid and formaldehyde were considered as major products for CO_2 reduction assisted by randomly oriented Co_3O_4 nanocrystals [40], while formate was the only product using highly textured {121} nanostructured Co_3O_4 [41]. However, Mendoza et al. [40] only used a small wavelength range in the visible spectrum (510 to 620 nm), neglecting the much wider absorption range (from UV to NIR) of this material. In the work of Huang et al. [41], the CO_2 photocatalytic reduction was assisted by an external electric potential in a photoelectrochemical cell configuration, adding additional energy to that of the radiation. These reasons make it interesting to explore the possibilities that can be offered by an abundant, inexpensive, and stable material such as Co_3O_4 when it is only excited with solar light irradiation. Thus, here we report the properties of Co_3O_4 . Herein, two different morphologies of this oxide were prepared based on synthesis procedures previously published. They were used as a heterogeneous catalyst for photochemical reactions with CO_2 and H_2O under artificial solar light irradiation, in order to evaluate their catalytic capabilities to generate hydrocarbons. In this work, the photocatalytic activity of Co_3O_4 (nanoparticles and porous structure) was evaluated for CO_2 reduction in water and under visible light. The photocatalytic reactions were carried out in aqueous dispersions without the use of sacrificial agents, under normal conditions, i.e., room temperature and atmospheric pressure.

2. Experimental

2.1. Preparation of Co_3O_4 Nanoparticles (Co_3O_4 -NPs) Photocatalyst. The synthesis of these nanoparticles was accomplished using an analogous method to that reported by Xie et al. [42]. Briefly, 1.19 g of $\text{CoCl}_2 \cdot 6\text{H}_2\text{O}$ (Mallinckrodt Pharmaceuticals, 99.63%) was added to 30 mL of ethylene glycol (EG) (Analytika, 99.1%), and the suspension was stirred and gradually heated to 80°C. Then, 100 mL of a 0.2 M solution of Na_2CO_3 (Reproquifin, 99% min.) in deionized water (15 M Ω cm) was added dropwise and the mixture was further aged for 1 h under argon gas (Praxair, grade 4.8, extra pure, 99.998% min.). The purple solid obtained was filtered, washed several times with deionized water until neutralization, and dried overnight at 100°C under vacuum. The obtained purple powder was characterized using powder X-ray diffraction (PXRD) and infrared (IR) spectroscopy.

As shown in Figure S1 it corresponds to cobalt hydroxycarbonate [43]. Finally, the solid was calcined for 4 h at 450°C, obtaining a black powder.

2.2. Preparation of a Porous and Nanostructured Co_3O_4 (Co_3O_4 -P-NS) Photocatalyst. This sort of cobalt (II, III) oxide was synthesized using the gel-combustion method, similarly to that previously reported by Makhlof et al. [44]. In our case, the quantities used were 1.46 g of $\text{Co}(\text{NO}_3)_2 \cdot 6\text{H}_2\text{O}$ (Ferromont, 99.6%) and 2.5 g of glycine (Sigma-Aldrich, 99%). Both powders were dissolved in 100 mL of deionized water under vigorous stirring. 3 mL of concentrated HNO_3 (J. T. Baker, 65.8%) was added when both powders were completely dissolved, and the heating of this reaction mixture started at 300°C. A purple gel was formed when almost all the water was evaporated, and then the temperature was increased up to 400°C. Finally, the combustion of the organic material took place and a black solid was obtained. The PXRD pattern is shown in Figure S2. After that, the solid was calcined for 4 h at 700°C in order to obtain the final material.

2.3. Characterization Techniques of the Photocatalysts. PXRD patterns were taken on a Bruker D2-Phaser diffractometer equipment using $\text{Cu K}\alpha$ radiation (10 mA, 30 kV, $\lambda = 1.5418 \text{ \AA}$) and an integration time of 0.5 s. Raman spectra were recorded with an EZRaman-N (Enwave Optronics Inc.) Raman analyzer coupled to a Leica DM300 microscope with a 40x objective, using an excitation laser source of 532 (~30 mW) or 905 (~160 mW) nm wavelengths. The infrared spectra were collected on a PerkinElmer Spotlight 400 FT-IR-FIR spectrometer with a Universal ATR sampling accessory. UV-visible-NIR electronic absorption spectra (under a diffuse reflectance regime) were recorded on a Varian Cary 5E, and the Kubelka-Munk function was computed. The transmission electron microscopy (TEM) micrograph and the selected area electron diffraction (SAED) pattern were obtained using a JEOL JEM-2012 microscope operating at a voltage of 200 kV. The scanning electron microscopy (SEM) images were obtained using a field-emission scanning electron microscope, JEOL JSM-5900-LV, operating at 20 kV. This microscope is equipped with an Oxford-ISIS for elemental analysis using energy-dispersive spectroscopy (EDS). The magnetic hysteresis loops (M–H) were measured in a vibrating sample magnetometer (VSM-LDJ 9600, 30,000 Oe) at room temperature with a standard magnetization curve routine. BET measurements were carried out by N_2 at –196°C in a Quantacore Nova 2000. Before the physisorption, the samples were degassed for 12 h at 150°C. XPS was performed in a spectrometer equipped with an Al $\text{K}\alpha$ X-ray source of 1486.6 eV. The analyzer energy was 23.5 eV and the base pressure was about 4.5×10^{-8} Pa.

2.4. Light Irradiation of CO_2 Bubbled in Water in the Presence of a Photocatalyst. In a general procedure, 20 mL of deionized water in a Schlenk vessel were bubbled for 1 h with gaseous CO_2 (Praxair, grade 3.0, 99.9%) in order to saturate water with CO_2 . Then, 4.15×10^{-2} mmol of a photocatalyst (Co_3O_4 -NPs or Co_3O_4 -P-NS) was suspended in the CO_2 solution. A stirring bar was introduced, the glass vessel was

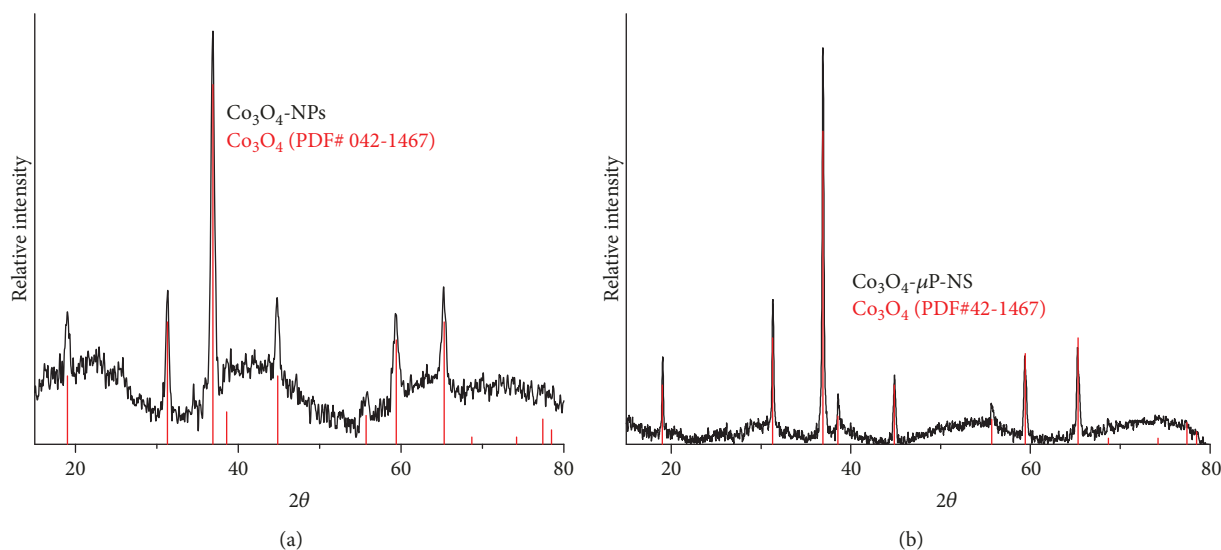


FIGURE 1: PXRD patterns of pure (a) Co_3O_4 -NPs and (b) Co_3O_4 -P-NS.

sealed, and the irradiation was carried out with a 150 W arc xenon lamp (Osram XBO 150 W/CR OFR), which roughly simulates the solar spectrum. The lamp was located at a distance from the vessel so that 100 mW/cm^2 of intensity was reached; a calibrated silicon photodiode (Thorlabs SM05PD2B) was used for that purpose. The experiments were accomplished at room temperature. After 6 hours of irradiation, the produced gases were collected in a Tedlar® bag and the resultant gaseous mixture was analyzed by gas chromatography (GC) in an Agilent 6890 series gas chromatograph with a 30-meter PerkinElmer PE-5 column ((5%-phenyl)-methylpolysiloxane). The temperature of the injector was 100°C , the oven was at 100°C , and the FID detector was at 150°C . Note that all the dispersions were prepared in deionized water. All the experiments were performed at least twice.

3. Results and Discussion

3.1. Characterization of Co_3O_4 -NPs and Co_3O_4 -P-NS. The powder diffraction pattern of the Co_3O_4 -NP sample, displayed in Figure 1(a), agrees well with that of Co_3O_4 (PDF no. 42-1467). The synthesized nanoparticles have cubic symmetry and its space group is Fd-3m. In this material, the lattice is formed with mixed-valence cobalt: Co^{2+} (33%) and Co^{3+} (66%). It has a spinel structure where the atoms of Co^{2+} are in a tetrahedral coordination and the atoms of Co^{3+} are in an octahedral coordination with oxygen atoms. The average crystallite size of Co_3O_4 -NPs estimated from the full width at half maximum of the (311) diffraction peak by applying the Scherrer equation is about 15 nm. The PXRD pattern of the prepared particles indicates the formation of the single spinel phase without any observable traces of cobalt hydroxide or cobalt monoxide. When Co_3O_4 -P-NS was synthesized by combustion, the dark grey solid obtained was also analyzed by PXRD. A mixture of Co_3O_4 , CoO, and Co was identified in the corresponding diffractogram

(Figure S2). This is due to the presence of reducing and oxidizing species in the combustion reaction. The average crystallite size, obtained by the same method used for the Co_3O_4 -NPs, was 21 nm. After the solid was calcined for 4 h at 700°C , as can be observed in Figure 1(b), the diffractogram only shows the Co_3O_4 cubic phase (PDF no. 42-1467) and its space group is Fd-3m. Due to the calcination process, the crystallite size increased to 45 nm. When the sample was annealed, the presence of Co and CoO was not detected, showing the formation of the single spinel phase. It is important to mention that the shape of the baseline in both diffractograms is due to the mathematical subtraction of the background, in order to remove the distortion produced by the fluorescence generated in the interaction of the Cu K α radiation with the Co atoms.

The electronic absorption spectrum of Co_3O_4 -NPs in the UV-visible-NIR region, using the diffuse reflectance mode displayed in Figure 2(a), shows different bands. Using Tauc's plot, different band gap energies were calculated. In the present study, the best fit of $(\alpha h\nu)^{1/n}$ versus photon energy was obtained for $n = 1/2$ for Co_3O_4 -NPs, which corresponds to direct band gap transitions. Then, the obtained gap energy values for Co_3O_4 -NPs were 0.78, 1.55, and 2.19 eV (see Figure 2(b)). The transition at 0.78 eV was recently attributed to a direct dipole-dipole forbidden d-d transition between the tetrahedral site of Co^{2+} cations [38]. The gaps at 1.55 and 2.19 eV are direct allowed transitions. These transitions are assigned to a charge transfer $\text{O}^{2-} \rightarrow \text{Co}^{3+}$ (the former) and a transition $\text{O}^{2-} \rightarrow \text{Co}^{2+}$ (the latter) [45–49]. The corresponding spectrum of Co_3O_4 -P-NS in Figure 2(c) shows, as in the case of Co_3O_4 -NPs, different direct band gap transitions. Using Tauc's plot, the calculated band gap energies for Co_3O_4 -P-NS (Figure 2(d)) were 1.96, 1.48, and 0.76 eV. The band gap values found for the Co_3O_4 -NP sample are slightly higher than those of the Co_3O_4 -P-NS. This fact could be due to a small quantum confinement effect in the Co_3O_4 -NPs

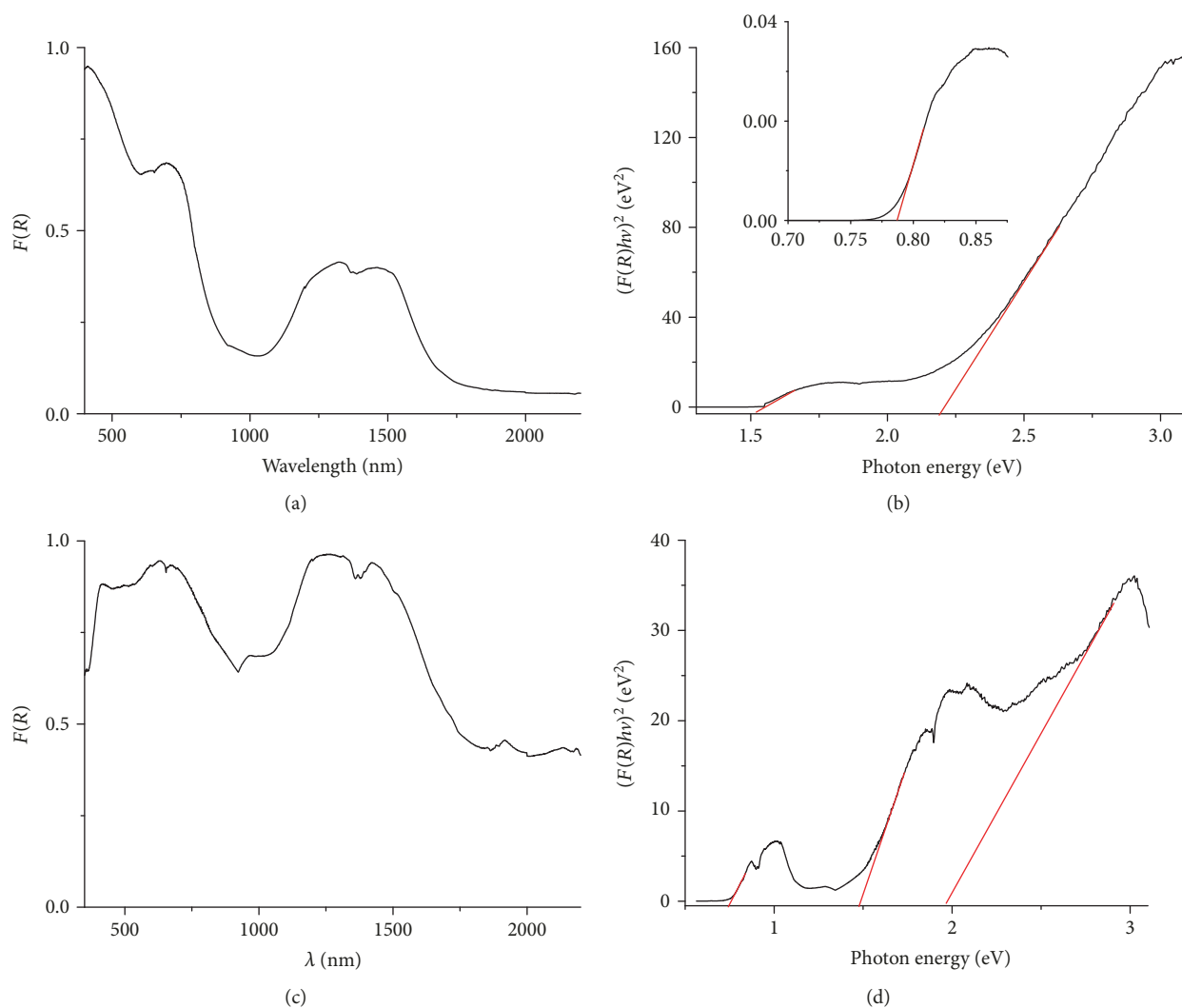


FIGURE 2: The electronic absorption spectra in the UV-visible-NIR region using the diffuse reflectance mode of (a) Co_3O_4 -NPs (black powder) and (c) Co_3O_4 -P-NS (dark grey powder). $(F(R)hv)^2$ vs. photon energy plot of (b) Co_3O_4 -NPs (two direct band gaps, 2.19 and 1.55 eV, were found in the main plot, and the insertion shows the third band gap, 0.78 eV) and (d) Co_3O_4 -P-NS (three direct band gaps, 1.96, 1.48, and 0.76 eV, were determined).

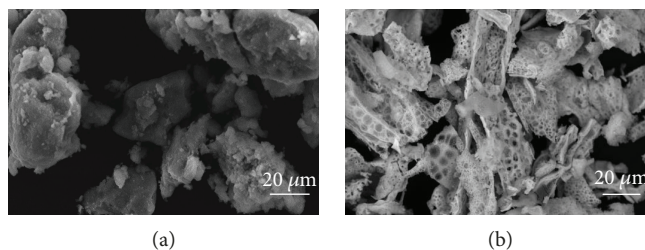


FIGURE 3: SEM micrographs of (a) Co_3O_4 -NPs and (b) Co_3O_4 -P-NS.

[50, 51]; this is in accordance with the smaller crystallite size observed in the PXRD analysis. In addition, the colors of the two powders are different (Figure S5): the nanoparticles are black and the porous material is dark grey.

A representative SEM micrograph of the Co_3O_4 -NP sample is shown in Figure 3(a). Considering the crystallite size

obtained for this sample (15 nm), the observed microstructures in Figure 3(a) must be composed of “nanoblocks.” In the SEM image of Co_3O_4 -P-NS (Figure 3(b)), large nanostructured arrays (crystallite size about 45 nm) with different pore sizes are observed. In this sample, the size of the observed pores are in the order of microns; this can be due

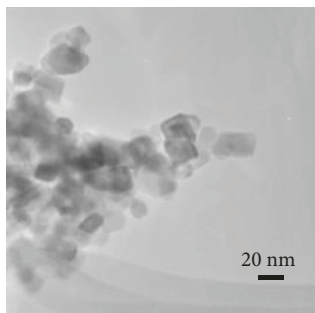


FIGURE 4: TEM image of Co_3O_4 -NPs.

to the high volume of gases produced during the combustion reaction [44].

It is clearly revealed in the TEM micrograph of Figure 4 that the microstructures observed in Figure 3(a) are in fact Co_3O_4 -NP porous agglomerates with a size in the order of submicrons. The corresponding pore sizes are in the range of 5–15 nm. These nanoparticles are agglomerated and have a rectangular shape and a mean size of 15.1 ± 3.6 nm (Figure S12). This value fairly matches the crystallite size found from the PXRD analysis.

For more details about the composition and structural characterization of the materials, see the supplementary materials.

3.2. Photocatalytic CO_2 Reduction. After characterization, the materials were dispersed in CO_2 -saturated water and irradiated. The purpose of our work was to evaluate the catalytic activity of the catalysts under normal conditions of temperature, pressure, and quantity of CO_2 determined by the solubility of the gas in water at atmospheric pressure. The reader can find elsewhere [52] more information about the different equilibria related to the solubility of CO_2 in water at different pH values; thus, the starting pH of the reaction solution was between 4.5 and 5. It is important to note that no sacrificial agent was used in the reaction. The collected gases were analyzed with a gas-chromatograph with a FID detector. Figure 5(a) shows the sharp band of the gas obtained after irradiation of the reaction suspension containing either Co_3O_4 -NPs or Co_3O_4 -P-NS. These peaks matched well with those corresponding to the methanol standard. As can be seen, the gas obtained with the two materials is the same, since the signal appears at the same retention time as that of methanol. Though this material has been widely used for water splitting and water oxidation, this is the first time MeOH production is reported when Co_3O_4 is used as a photocatalyst in a system as described herein. It is noteworthy that the reaction product obtained here is different from those reported in the two previous works using Co_3O_4 as a photocatalyst, which at the same time are different from each other [40, 41]. This apparent discrepancy may be explained, since different excitation conditions were used in every report: (i) In the work of Mendoza et al. [40], the irradiation was carried out using a small window of the visible spectrum (510 to 620 nm); the light intensity in the reaction medium was not reported. (ii) In the report of Huang et al. [41], a Xe lamp was used to irradiate the reaction system at an

intensity of 9 mW/cm^2 and the photoelectrode was polarized at 0.9 V (vs. SCE) during the experiments. (iii) In our case, the intensity of the irradiation in the reaction system was 100 mW/cm^2 , coming from a Xe arc lamp typically used in solar simulators. These different excitation conditions, together with slightly different light absorption capabilities, cause different concentrations of photogenerated carriers, different Fermi level positions, and consequently, different potential distributions across the semiconductor/electrolyte interface [53]. Thus, different reactions could be expected. The exposed planes of the materials could make a difference too, with regard to the photocatalytic activity. It is well known that the plane (110) mainly contains Co^{3+} ions in an octahedral coordination that are good for the oxidation of, e.g., CO and alcohols [42, 54, 55]. Also, the planes (001) and (111) mainly contain Co^{2+} ions in a tetrahedral coordination that are almost inactive for the oxidation [56–58]. It is worth saying that the plane (111) is the one that we found in the HR-TEM images. Other possible reasons, like different relative band positions, different electrolyte compositions affecting the redox equilibrium, and different Co_3O_4 crystalline textures affecting the corresponding surface activities, cannot be discarded.

For the products obtained in this work, the signals obtained were used by means of qualitative detection, not for quantitative purposes, due to the fact that very small amounts of them were obtained in these studies [59, 60]. Attempts to fully characterize MeOH in the remnant solution were unsuccessful due to the lower amounts of gas produced. The fact that methanol was detected as a gas and none was detected in the remnant solution is not surprising. This is probably due to the fact that the methanol produced in the reaction evaporated, since the reaction solution reaches 35°C upon irradiation and atmospheric pressure in our room conditions is 585 mm Hg. A possible general mechanism explaining the photoreduction of CO_2 and the production of methanol can be seen in Figure 5(b). As it is well known, the reduction of CO_2 to methanol needs protons and electrons. In our experimental conditions, there are two possible proton sources: (1) the oxidation of water with Co_3O_4 and the production of H^+ [61] and (2) the dissociation equilibrium of $\text{H}_2\text{CO}_3/\text{HCO}_3^-$ [62, 63]. For the initial pH values encountered in the solution reaction (4.5–5), the expected species are $\text{CO}_2(\text{aq})$, H_2CO_3 , and a small quantity of HCO_3^- in equilibrium with the carbonic acid. In the literature, it is reported that the concentration of $\text{CO}_2(\text{aq})$ in a solution is approximately 500 times the concentration of H_2CO_3 in standard reaction conditions [63]. As mentioned above, the pH determines the species you can find and their concentration in the solution. That is, the concentration of H_2CO_3 in a solution is from 23 to 71 times greater than the concentration of HCO_3^- ; consequently, the concentration of $\text{CO}_2(\text{aq})$ is from 11,500 to 35,500 times larger than the concentration of HCO_3^- (the calculations are developed in Appendix A of the supporting information). Considering the different carbon-containing species present in the reaction medium and their corresponding potential reduction (see Figure 6), we suggest that at least two pathways in the formation of methanol are possible. One path is where

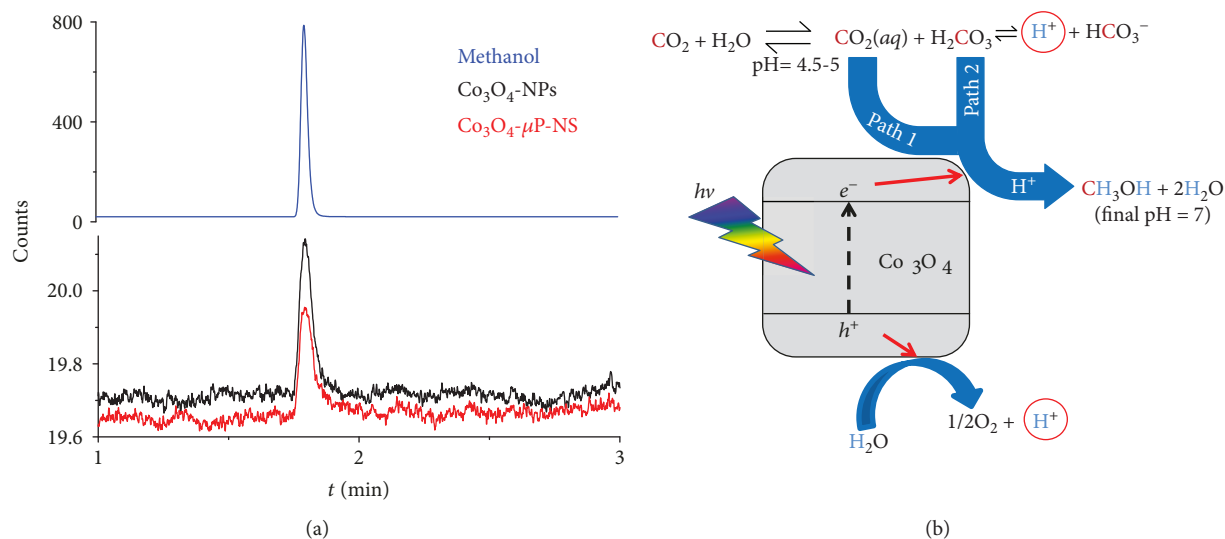


FIGURE 5: (a) Chromatograms of the gas obtained after visible-light irradiation with Co₃O₄-NPs and Co₃O₄-P-NS as catalysts; the blue trace corresponds to the chromatogram of the methanol reference; (b) general mechanism explaining the photoreduction of CO₂ to MeOH catalysed by both types of Co₃O₄ nanostructures.

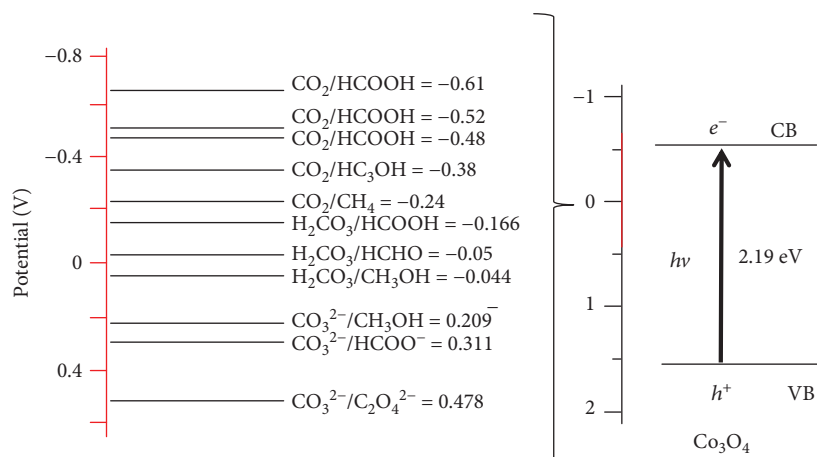


FIGURE 6: Scheme of redox potentials for CO₂, carbonates, and Co₃O₄. The potential scales were obtained vs. NHE at pH = 7 [62].

CO₂(aq) is combined with protons and photogenerated electrons to produce methanol, and the other path is where carbonic acid is combined with protons and reduced to give MeOH. In terms of the concentration of the two species, the former pathway is favored because the concentration of CO₂(aq) is 500 higher than that of the H₂CO₃ in solution; however, in thermodynamic terms, the second path is preferred because the reduction potential of the H₂CO₃/CH₃OH pair is more positive than that of CO₂/CH₃OH (Figure 6). We do not have enough experimental evidences to establish which of these two possible mechanisms has a higher contribution.

For the Co₃O₄-NPs, the highest direct gap energy transition is 2.19 eV, while that of Co₃O₄-P-NS is 1.96 eV. In Figure 6, the redox potentials of different possible products are shown. Taking into account the band gap obtained for our materials, methanol production, and possible water oxidation [61], it is possible to assume that the conduction band

could be more reductive than the redox potential of the CO₂/CH₃OH pair and the valence band might be more oxidizing than the oxidation potential of the water.

By preparing two different morphologies of Co₃O₄, it was expected to obtain different products, quantities, or both. Nevertheless, no significant differences were observed between the two morphologies regarding their photocatalytic behavior. It is important to mention that CO₃²⁻ anions are not formed in the pH range of our experiments. At the end of the experiment, the pH of the remnant solution was 7, which means that the concentration of dissolved CO₂ (or the H₂CO₃/HCO₃⁻ pair) significantly decreased in the solution.

Once the reaction was completed, the materials were collected with a centrifuge and dried in a vacuum oven at 80°C overnight. After that, the PXRD of the two materials were recorded again (Figure S16(a) and S16(b)). When the average size of a crystallite was calculated for Co₃O₄-NPs, it increased from 19 nm to 21 nm. For Co₃O₄-P-NS, the

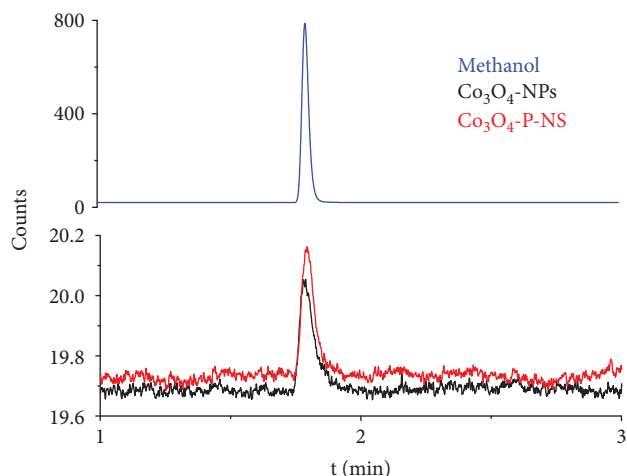


FIGURE 7: Chromatograms of the gases obtained after reutilizing Co_3O_4 -NPs (black line) and Co_3O_4 -P-NS (red line) compared with that of the methanol standard (blue line).

crystallite size increased from 45 nm to 51 nm. Considering that the smallest particles could be retained in the final reaction solution, the increase of the crystallite was not significant in the two cases. In addition, no signal of cobalt hydroxides or carbonates was observed, so the materials did not change in composition or in size by means of PXRD. No changes were observed in their Raman spectrum either (Figure S16(c) and S16(d)). These results indicate that no significant changes in the structure of the catalysts were produced after the first cycle. Moreover, the optical properties remained unaltered (not shown).

The reaction was carried out again under the same conditions as the experiment mentioned above, using the recovered catalytic materials. Even more interesting was to corroborate that those materials conserved their activity for the reduction of CO_2 . As can be seen in Figure 7, the chromatograms revealed that methanol was obtained again with the reutilized materials.

After the second cycle, we tried to recover the catalysts in order to characterize the structural and optical properties to evaluate possible changes, but we did not succeed. The solids remained stuck on the walls of the reactor.

It is worth mentioning that the viability of these catalysts for long-term use is still under investigation.

4. Conclusions

We have an unprecedented report of methanol production using a photocatalytic system with a very simple architecture working under ordinary reaction conditions. Co_3O_4 nanostructures showed photocatalytic activity in the CO_2 reduction process, and methanol is the only detected reaction product. It is possible to assert that this is a simple example of artificial photosynthesis. Co_3O_4 has been widely used for water splitting and water oxidation, but this is the first time MeOH production is reported when this material is used as a photocatalyst.

Co_3O_4 -NPs and Co_3O_4 -P-NS were satisfactorily synthesized by adding changes to two reported methods. No

impurities were detected in the synthesized Co_3O_4 -P-NS powder. A small quantum confinement was found for the two samples compared with the bulk material, being higher for Co_3O_4 -NPs. No significant differences were observed between the two reported morphologies regarding the photocatalytic behavior.

Data Availability

The data used to support the findings of this study are included within the article and the supplementary information files.

Disclosure

Inti Zumeta-Dube's current address is Centro de Investigación en Ciencia Aplicada y Tecnología Avanzada, Unidad Legaria, Instituto Politécnico Nacional, Calzada Legaria No. 694, Col. Irrigación, Del. Miguel Hidalgo, CP 11500, México D.F., Mexico.

Conflicts of Interest

The authors declare that there is no conflict of interest regarding this publication of this paper.

Acknowledgments

This research has received partial funding from the European Community's Seventh Framework Programme (FP7-NMP-2010-EU-MEXICO) and CONACYT (BisNano), under Grant Agreement nos. 263878 and 125141, respectively. Inti Zumeta-Dube is grateful to CONACYT (project number 174247), ICYTDF, BisNano, and the project CM-SECITI/095/2017 "Planta piloto sustentable operada con energía solar para el tratamiento de agua pluvial de la CDMX" for the postdoctoral fellowship. Salvador Pocoví-Martínez is thankful for the postdoctoral fellowship from DGAPA-UNAM. David Diaz thanks DGAPA-UNAM (IN115212 and IN116214 PAPIIT projects) and CONACYT (Redes193850 and SEP-CB-132094 projects) for the financial support. The authors want to thank Dr. Edilso Reguera-Ruiz (CICATA-U Legaria, IPN), Dr. Aida Gutiérrez Alejandre (FQ-UNAM), and Dr. Tobías Noel Nava-Entzama (IMP) for the access to several instrumental facilities.

Supplementary Materials

Figure S1: (a) XRD pattern and (b) IR spectrum of $\text{CoCO}_3(\text{OH})_2$. Figure S2: XRD pattern of the black solid after combustion. Figure S3: Raman spectra recorded using a wavelength excitation laser source of 532 nm for (a) Co_3O_4 -NPs and (b) Co_3O_4 -P-NS. Figure S4: IR spectra of (a) Co_3O_4 -NPs and (b) Co_3O_4 -P-NS. Figure S5: pictures of (a) Co_3O_4 -NPs and (b) Co_3O_4 -P-NS powders. Figure S6: EDS spectra of (a) Co_3O_4 -NPs and (b) Co_3O_4 -P-NS. Figure S7: SEM images of Co_3O_4 -NPs. Figure S8: SEM images of Co_3O_4 -NPs. Figure S9: SEM images of Co_3O_4 -NPs. Figure S10: (a) HR-TEM, (b) FFT of the framed region, and (c) reciprocal lattice of 2 different zones of Co_3O_4 -NPs. Figure S11: (a)

SAED pattern and (b) unit cell representation of Co_3O_4 -NPs. Figure S12: size distribution of Co_3O_4 -NPs. Figure S13: magnetization curve of (a) Co_3O_4 -NPs and (b) Co_3O_4 -P-NS. Figure S14: XPS of Co_3O_4 -NPs: (a) wide-range spectra and high-resolution spectra of (b) Co2p, (c) C1s, and (d) O1s. Figure S15: isotherm plot for adsorption-desorption of (a) Co_3O_4 -NPs and (c) Co_3O_4 -P-NS; BET surface area plot of (b) Co_3O_4 -NPs and (d) Co_3O_4 -P-NS. Figure S16: XRD patterns and Raman spectrum after photocatalytic reaction of (a, c) Co_3O_4 -NPs and (b, d) Co_3O_4 -P-NS. Appendix A: calculation of the different concentration relations of species in solution. (*Supplementary Materials*)

References

- [1] M. Watanabe, H. Shiogama, H. Tatebe, M. Hayashi, M. Ishii, and M. Kimoto, "Contribution of natural decadal variability to global warming acceleration and hiatus," *Nature Climate Change*, vol. 4, no. 10, pp. 893–897, 2014.
- [2] R. P. Allan, *Nature*, vol. 470, no. 7334, pp. 344–345, 2011.
- [3] P. I. Palmer and M. J. Smith, "Earth systems: model human adaptation to climate change," *Nature*, vol. 512, no. 7515, pp. 365–366, 2014.
- [4] P. H. Carr, "Weather extremes from anthropogenic global warming," *Natural Science*, vol. 5, no. 1, pp. 130–134, 2013.
- [5] S. Rahmstorf and A. Ganopolski, "Long-term global warming scenarios computed with an efficient coupled climate model," *Climatic Change*, vol. 43, no. 2, pp. 353–367, 1999.
- [6] R. Assel, "Implications of CO_2 global warming on Great Lakes ice cover," *Climatic Change*, vol. 18, no. 4, pp. 377–395, 1991.
- [7] F. Cherubini, G. P. Peters, T. Berntsen, A. H. Strømman, and E. Hertwich, " CO_2 emissions from biomass combustion for bioenergy: atmospheric decay and contribution to global warming," *GCB Bioenergy*, vol. 3, no. 5, pp. 413–426, 2011.
- [8] P. M. Cox, R. A. Betts, C. D. Jones, S. A. Spall, and I. J. Totterdell, "Acceleration of global warming due to carbon-cycle feedbacks in a coupled climate model," *Nature*, vol. 408, no. 6809, pp. 184–187, 2000.
- [9] D. S. Jenkinson, D. E. Adams, and A. Wild, "Model estimates of CO_2 emissions from soil in response to global warming," *Nature*, vol. 351, no. 6324, pp. 304–306, 1991.
- [10] A. Yamasaki, "An overview of CO_2 mitigation options for global warming—emphasizing CO_2 sequestration options," *Journal of Chemical Engineering of Japan*, vol. 36, no. 4, pp. 361–375, 2003.
- [11] P. R. Jeon, J. Choi, T. S. Yun, and C.-H. Lee, "Sorption equilibrium and kinetics of CO_2 on clay minerals from subcritical to supercritical conditions: CO_2 sequestration at nanoscale interfaces," *Chemical Engineering Journal*, vol. 255, pp. 705–715, 2014.
- [12] B. H. Jo, J. H. Seo, and H. J. Cha, "Bacterial extremophilic carbonic anhydrases from deep-sea hydrothermal vents as potential biocatalysts for CO_2 sequestration," *Journal of Molecular Catalysis B: Enzymatic*, vol. 109, pp. 31–39, 2014.
- [13] I. Criscuolo, G. Alberti, S. Baronti et al., "Carbon sequestration and fertility after centennial time scale incorporation of charcoal into soil," *PLoS One*, vol. 9, no. 3, article e91114, 2014.
- [14] O. Rahmani, R. Junin, M. Tyrer, and R. Mohsin, "Mineral carbonation of red gypsum for CO_2 sequestration," *Energy & Fuels*, vol. 28, no. 9, pp. 5953–5958, 2014.
- [15] S. García, Q. Liu, and M. M. Maroto-Valer, "A novel high pressure-high temperature experimental apparatus to study sequestration of CO_2 - SO_2 mixtures in geological formations," *Greenhouse Gases: Science and Technology*, vol. 4, no. 4, pp. 544–554, 2014.
- [16] J. D. McDonald, D. Kracko, M. Doyle-Eisele et al., "Carbon capture and sequestration: an exploratory inhalation toxicity assessment of amine-trapping solvents and their degradation products," *Environmental Science & Technology*, vol. 48, no. 18, pp. 10821–10828, 2014.
- [17] C. Burrows and M. Appold, "Hydrology of the Forest City basin, mid-continent, USA: implications for CO_2 sequestration in the St. Peter Sandstone," *Environmental Earth Sciences*, vol. 73, no. 4, pp. 1409–1425, 2015.
- [18] L. Mendes, J. de Medeiros, R. B. Alves, and O. F. Araújo, "Production of methanol and organic carbonates for chemical sequestration of CO_2 from an NGCC power plant," *Clean Technologies and Environmental Policy*, vol. 16, pp. 1095–1105, 2014.
- [19] P. Baran, K. Zarębska, and A. Nodzeński, "Energy aspects of CO_2 sorption in the context of sequestration in coal deposits," *Journal of Earth Science*, vol. 25, no. 4, pp. 719–726, 2014.
- [20] Y. Lee, S. Lee, Y. K. Jin, and Y. Seo, "1-Propanol as a co-guest of gas hydrates and its potential role in gas storage and CO_2 sequestration," *Chemical Engineering Journal*, vol. 258, pp. 427–432, 2014.
- [21] S. Coşkun, Z. Taşçı, M. Ulusoy, and M. Yurdakoç, "Catalytic conversion of carbon dioxide into cyclic carbonates by Cu(II) and Ni(II) acetylacetonates anchored onto Siral 80," *Turkish Journal of Chemistry*, vol. 38, pp. 600–610, 2014.
- [22] W. Queen, M. Hudson, E. Bloch et al., "Comprehensive study of carbon dioxide adsorption in the metal-organic frameworks M_2 (dobdc) ($\text{M} = \text{Mg}, \text{Mn}, \text{Fe}, \text{Co}, \text{Ni}, \text{Cu}, \text{Zn}$)," *Chemical Science*, vol. 5, no. 12, pp. 4569–4581, 2014.
- [23] X. Meng, T. Wang, L. Liu et al., "Photothermal conversion of CO_2 into CH_4 with H_2 over group VIII nanocatalysts: an alternative approach for solar fuel production," *Angewandte Chemie, International Edition*, vol. 53, pp. 1478–1482, 2014.
- [24] S. Walspurger, W. G. Haije, and B. Louis, " CO_2 reduction to substitute natural gas: toward a global low carbon energy system," *Israel Journal of Chemistry*, vol. 54, no. 10, pp. 1432–1442, 2014.
- [25] P. Mohanty, K. K. Pant, S. N. Naik, J. Parikh, A. Hornung, and J. N. Sahu, "Synthesis of green fuels from biogenic waste through thermochemical route—the role of heterogeneous catalyst: a review," *Renewable and Sustainable Energy Reviews*, vol. 38, pp. 131–153, 2014.
- [26] J. L. White, J. T. Herb, J. J. Kaczur, P. W. Majsztrik, and A. B. Bocarsly, "Photons to formate: efficient electrochemical solar energy conversion via reduction of carbon dioxide," *Journal of CO_2 Utilization*, vol. 7, pp. 1–5, 2014.
- [27] K. Sun, S. Shen, Y. Liang, P. E. Burrows, S. S. Mao, and D. Wang, "Enabling silicon for solar-fuel production," *Chemical Reviews*, vol. 114, no. 17, pp. 8662–8719, 2014.
- [28] H.-Y. Wang, D. Bluck, and B. J. Van Wie, "Conversion of microalgae to jet fuel: process design and simulation," *Biore-source Technology*, vol. 167, pp. 349–357, 2014.
- [29] G. Sneddon, A. Greenaway, and H. H. P. Yiu, "The potential applications of nanoporous materials for the adsorption, separation, and catalytic conversion of carbon dioxide," *Advanced Energy Materials*, vol. 4, no. 10, article 1301873, 2014.

- [30] W. Tu, Y. Zhou, and Z. Zou, "Photoconversion: photocatalytic conversion of CO₂ into renewable hydrocarbon fuels: state-of-the-art accomplishment, challenges, and prospects (Adv. Mater. 27/2014)," *Advanced Materials*, vol. 26, no. 27, pp. 4598–4598, 2014.
- [31] L. M. Aeshala, R. Uppaluri, and A. Verma, "Electrochemical conversion of CO₂ to fuels: tuning of the reaction zone using suitable functional groups in a solid polymer electrolyte," *Physical Chemistry Chemical Physics*, vol. 16, no. 33, pp. 17588–17594, 2014.
- [32] M. Bevilacqua, J. Filippi, A. Lavacchi et al., "Energy savings in the conversion of CO₂ to fuels using an electrolytic device," *Energy Technology*, vol. 2, no. 6, pp. 522–525, 2014.
- [33] M. H. Wilson, J. Groppo, A. Placido et al., "CO₂ recycling using microalgae for the production of fuels," *Applied Petrochemical Research*, vol. 4, no. 1, pp. 41–53, 2014.
- [34] Y. Izumi, "Recent advances in the photocatalytic conversion of carbon dioxide to fuels with water and/or hydrogen using solar energy and beyond," *Coordination Chemistry Reviews*, vol. 257, no. 1, pp. 171–186, 2013.
- [35] M. J. Kenney, M. Gong, Y. Li et al., "High-performance silicon photoanodes passivated with ultrathin nickel films for water oxidation," *Science*, vol. 342, no. 6160, pp. 836–840, 2013.
- [36] W.-E. Wang, J. Soulis, Y. J. Yang, and P. Biswas, "Comparison of CO₂ photoreduction systems: a review," *Aerosol and Air Quality Research*, vol. 14, no. 2, pp. 533–549, 2014.
- [37] J. Chen and A. Selloni, "Electronic states and magnetic structure at the Co₃O₄(110) surface: a first-principles study," *Physical Review B*, vol. 85, no. 8, article 085306, 2012.
- [38] L. Qiao, H. Y. Xiao, H. M. Meyer et al., "Nature of the band gap and origin of the electro-/photo-activity of Co₃O₄," *Journal of Materials Chemistry C*, vol. 1, no. 31, pp. 4628–4633, 2013.
- [39] J. Chen, X. Wu, and A. Selloni, "Electronic structure and bonding properties of cobalt oxide in the spinel structure," *Physical Review B*, vol. 83, no. 24, article 245204, 2011.
- [40] J. Mendoza, H. Kim, H. Park, and K. Park, "Photocatalytic reduction of carbon dioxide using Co₃O₄ nanoparticles under visible light irradiation," *Korean Journal of Chemical Engineering*, vol. 29, no. 11, pp. 1483–1486, 2012.
- [41] X. Huang, T. Cao, M. Liu, and G. Zhao, "Synergistic photoelectrochemical synthesis of formate from CO₂ on {121} hierarchical Co₃O₄," *The Journal of Physical Chemistry C*, vol. 117, no. 50, pp. 26432–26440, 2013.
- [42] X. Xie, Y. Li, Z.-Q. Liu, M. Haruta, and W. Shen, "Low-temperature oxidation of CO catalysed by Co₃O₄ nanorods," *Nature*, vol. 458, no. 7239, pp. 746–749, 2009.
- [43] R. Xu and H. C. Zeng, "Dimensional control of cobalt-hydroxide-carbonate nanorods and their thermal conversion to one-dimensional arrays of Co₃O₄ nanoparticles," *The Journal of Physical Chemistry B*, vol. 107, no. 46, pp. 12643–12649, 2003.
- [44] M. T. Makhlof, B. M. Abu-Zied, and T. H. Mansoure, "Direct fabrication of cobalt oxide nanoparticles employing sucrose as a combustion fuel," *Journal of Nanoparticles*, vol. 2013, Article ID 384350, 7 pages, 2013.
- [45] P. H. T. Ngamou and N. Bahlawane, "Influence of the arrangement of the octahedrally coordinated trivalent cobalt cations on the electrical charge transport and surface reactivity," *Chemistry of Materials*, vol. 22, no. 14, pp. 4158–4165, 2010.
- [46] N. Bahlawane, E. F. Rivera, K. Kohse-Höinghaus, A. Brechling, and U. Kleineberg, "Characterization and tests of planar Co₃O₄ model catalysts prepared by chemical vapor deposition," *Applied Catalysis B: Environmental*, vol. 53, no. 4, pp. 245–255, 2004.
- [47] L. D. Kadam and P. S. Patil, "Thickness-dependent properties of sprayed cobalt oxide thin films," *Materials Chemistry and Physics*, vol. 68, no. 1-3, pp. 225–232, 2001.
- [48] D. Barreca, C. Massignan, S. Daolio et al., "Composition and microstructure of cobalt oxide thin films obtained from a novel cobalt(II) precursor by chemical vapor deposition," *Chemistry of Materials*, vol. 13, no. 2, pp. 588–593, 2001.
- [49] H. Yamamoto, S. Tanaka, and K. Hirao, "Effects of substrate temperature on nanostructure and band structure of sputtered Co₃O₄ thin films," *Journal of Applied Physics*, vol. 93, no. 7, pp. 4158–4162, 2003.
- [50] N. Zhang, S. Jinwen, S. S. Mao, and L. Guo, "Co₃O₄ quantum dots: reverse micelle synthesis and visible-light-driven photocatalytic overall water splitting," *Chemical Communications*, vol. 50, no. 16, pp. 2002–2004, 2014.
- [51] A. K. Sarfraz and S. K. Hasanain, "Size dependence of magnetic and optical properties of Co₃O₄ nanoparticles," *Acta Physica Polonica A*, vol. 125, no. 1, pp. 139–144, 2014.
- [52] J. L. Ortiz-Quinónez, C. Vega-Verduga, D. Díaz, and I. Zumeta-Dubé, "Transformation of bismuth and β-Bi₂O₃ nanoparticles into (BiO)₂CO₃ and (BiO)₄(OH)₂CO₃ by capturing CO₂: the role of halloysite nanotubes and "sunlight" on the crystal shape and size," *Crystal Growth & Design*, vol. 18, no. 8, pp. 4334–4346, 2018.
- [53] H. O. Finklea, *Semiconductor Electrodes*, Elsevier, The University of Michigan, 1988.
- [54] A. Jha and C. V. Rode, "Highly selective liquid-phase aerobic oxidation of vanillyl alcohol to vanillin on cobalt oxide (Co₃O₄) nanoparticles," *New Journal of Chemistry*, vol. 37, no. 9, pp. 2669–2674, 2013.
- [55] V. R. Mate, M. Shirai, and C. V. Rode, "Heterogeneous Co₃O₄ catalyst for selective oxidation of aqueous veratryl alcohol using molecular oxygen," *Catalysis Communications*, vol. 33, pp. 66–69, 2013.
- [56] S. C. Petitto, E. M. Marsh, G. A. Carson, and M. A. Langell, "Cobalt oxide surface chemistry: the interaction of CoO(1 0 0), Co₃O₄(1 1 0) and Co₃O₄(1 1 1) with oxygen and water," *Journal of Molecular Catalysis A: Chemical*, vol. 281, no. 1-2, pp. 49–58, 2008.
- [57] K. Omata, T. Takada, S. Kasahara, and M. Yamada, "Active site of substituted cobalt spinel oxide for selective oxidation of COH₂. Part II," *Applied Catalysis A: General*, vol. 146, no. 2, pp. 255–267, 1996.
- [58] J. Jansson, A. E. C. Palmqvist, E. Fridell et al., "On the catalytic activity of Co₃O₄ in low-temperature CO oxidation," *Journal of Catalysis*, vol. 211, no. 2, pp. 387–397, 2002.
- [59] B. Pan, S. Luo, W. Su, and X. Wang, "Photocatalytic CO₂ reduction with H₂O over LaPO₄ nanorods deposited with Pt cocatalyst," *Applied Catalysis B: Environmental*, vol. 168–169, pp. 458–464, 2015.
- [60] Y. Liu, S. Zhou, J. Li et al., "Photocatalytic reduction of CO₂ with water vapor on surface La-modified TiO₂ nanoparticles with enhanced CH₄ selectivity," *Applied Catalysis B: Environmental*, vol. 168–169, pp. 125–131, 2015.
- [61] M. Zhang, M. de Respinis, and H. Frei, "Time-resolved observations of water oxidation intermediates on a cobalt oxide nanoparticle catalyst," *Nature Chemistry*, vol. 6, no. 4, pp. 362–367, 2014.

- [62] X. Yang, T. Xiao, and P. P. Edwards, "The use of products from CO₂ photoreduction for improvement of hydrogen evolution in water splitting," *International Journal of Hydrogen Energy*, vol. 36, no. 11, pp. 6546–6552, 2011.
- [63] D. C. Harris, *Quantitative Chemical Analysis*, W.H. Freeman and Company, New York, NY, USA, 7th edition, 2007.



Hindawi
Submit your manuscripts at
www.hindawi.com

